Numerical study of water ice and molecular contamination build up during JWST deployment

Lubos Brieda[a], Marc Laugharn[a], Michael Woronowicz[b], Kelly Henderson-Nelson[b], Christopher May[c], Eve Wooldridge[d]

[a]Particle in Cell Consulting LLC, Westlake Village, CA 91362, USA
[b]KBR Inc., Fulton, MD 20759, USA
[c]MAZE Engineering Solutions, Inc., Marshall, VA 20115
[d]NASA Goddard Space Flight Center, Greenbelt, MD 20771, USA

ABSTRACT

This paper summarizes a recent numerical analysis of water vapor and volatile condensible material deposition on the James Webb Space Telescope from the initial orbit insertion up to 180 days post launch. The analysis utilized 17 distinct geometry files capturing observatory configuration changes during the deployment. Surface temperature was set from a time-dependent thermal analysis solution. A vapor pressure model was used to calculate the net water ice adsorption. Molecular contamination included a contribution from UV photopolymerization. The analysis predicted levels of ice and molecular accumulation were found to be within the allowable limits specified by the observatory contamination control plan.

Keywords: spacecraft contamination, water ice buildup, numerical analysis

1. INTRODUCTION

Unlike its predecessor the Hubble Space Telescope, the James Webb Space Telescope (JWST), launched in late 2021, operates in the infrared regime. This design decision introduced the necessity to maintain low temperature in the vicinity of the detectors to prevent saturating the faint observed signal with a spurious thermal signature emanating from the spacecraft itself. This separation was accomplished by dividing the satellite into two parts: the cold "observatory" facing deep space, and the warm "spacecraft" facing the Sun. The interface is formed by the characteristic five layer sunshield membrane (or sunshield for short). The resulting thermal profile introduced an interesting wrinkle from the contamination control and systems engineering perspectives. Despite water being found on most surfaces, and water also being one of the primary constituents of material released by outgassing, the typical space mission does not concern itself with water vapor. The reason is that at the low pressures found in space, water requires temperatures around 150 K to freeze. The typical spacecraft utilizes on-board heaters in conjunction with a possible "rotisserie" in the sunshine to maintain surfaces within a narrow band around the standard room temperature. As such, ice formation is not a concern as any water molecules impacting the surface simply bounce off and fly off to space. The need to keep the observatory cold did not make it possible for JWST to achieve a similar thermal control. Shortly post launch, the spacecraft is rotated into the operational orientation with the observatory side facing away from the Sun. Even prior to the sunshield deployment, the observatory already begins cooling due to shadowing by the spacecraft structure. Although a rotation was scheduled to occur prior to the lowering of the "unitized pallet structure" (UPS) booms, the duration was not sufficient to lead to a significant warmup of the instrument deck itself.

The objective of this analysis was to determine the thickness of water ice, as well as "regular" molecular contaminant, that could be expected throughout the 180-day commissioning interval given the continuously changing surface temperature and outgassing rates. Performing the analysis required taking into account multiple geometrical configurations encountered during deployment, as it was possible that ice collected on a structure in one deployment stage is transported to a new physical location when that structure actuates where it may sublimate based on a new surface temperature. The work presented here updates a prior "Contamination Source

---

Corresponding author, lubos.brieda@particleincell.com

and Effects Analysis" (CSEA),[1] although the two analyses used different methodologies and numerical codes. We begin the paper by describing the legacy and the new numerical model. We then describe the vast family of inputs that had to be ingested by the analysis code. These included, among others, 17 different geometry files, seven large binary files providing temporal evolution of surface temperatures spanning the first 180 days from launch, and supplementary files aiding with material assignment. We also introduce outgassing and surface desorption models, and review numerical integration testing. The paper concludes by discussing results from the water vapor and molecular contamination transport analysis.

2. NUMERICAL MODEL

2.1 Contamination Transport

Fundamentally, computing molecular deposition involves determining how much material reaches, and sticks to, a surface element i due to outgassing from all other elements. Using the notation from the CSEA,[1] this can be written as

$$\dot{m}_i(t) = \sum_{j \neq i} \left[\nu_j(t) + \gamma_j(t) \right] A_j F_{ji} - \nu_i(t) \quad , i = 1, \ldots, N \tag{1}$$

where ν is the mass desorption rate (kg/s), γ is the surface outgassing rate (kg/s), A is the surface area (m^2), and F_{ji} is the area-normalized black-body "form factor". It specifies the fraction of molecules emitted from element j that reach element i without re-emission from a secondary surface. In other words, this equation states that time evolution of mass on element i is due to the outgassed and desorbed mass arriving from all other elements minus the mass desorbing from it. The time variation of surface mass can then be estimated by numerically integrating Equation 1 using a method such as the first order Forward Euler,

$$m_i(t + \Delta t) = m_i(t) + \dot{m}_i \Delta t \tag{2}$$

2.2 Legacy Approach

In order to utilize Equation 1, we need to define models for desorption and outgassing rates as a function of time and/or surface temperature. We also need values for the F_{ji} form factors between all surface elements. Given that a typical detailed geometry model may contain hundreds of thousands of such elements, filling the coefficients of this dense matrix is not trivial due to the N^2 dependence. The geometry models used for this analysis contained in excess of 100,000 surface elements each. Taking into account symmetry, filling out the form factor matrix involves calculating almost 5 billion coefficients.

In the legacy work, this computation was performed by an off-the-shelf radiation heat transfer code Thermal Synthesizer System (TSS).[2] At low gas densities, the mean distance between molecular collisions greatly exceeds the spacecraft dimensions. Molecules then bounce between surfaces without interacting with each other in a state known as *free molecular flow*. On surface impact, low velocity molecules reflect in a direction following the cosine law off the surface normal. This type of propagation is analogous to photons reflecting off a rough (diffuse) surface. For this reason, it is customary for the contamination control community to utilize radiative heat transfer codes such as TSS or Thermal Desktop to determine the view factors. Radiation heat transfer codes work by launching some large number of randomly oriented rays from each source node. The code then finds the first surface element intersected by the ray. Rays without an intersection correspond to the fraction of molecules lost to space. In thermal analysis, the computed form factors are subsequently utilized along with a conductivity network to establish surface temperature arising from radiative and conductive heat transport. In the case of molecular analysis, the form factors can be used to integrate the surface mass concentration. The actual integration of Equation 1 in the legacy CSEA analysis was achieved using in-house MolMAP and AquaMAP programs. The source code was not available but to the best of our understanding, these are Matlab (or similar) scripts that numerically integrate the mass deposition by repeatedly performing matrix-vector multiplications to march the solution forward using a scheme such as Forward Euler. At each time step, the time-varying surface temperature map is used to evaluate the material outgassing and desorption, ν and γ.

2.3 Updated Model

In this work we used a different approach. Specifically, we utilize an in-house developed Contamination Transport Simulation Program (CTSP).[3,4] CTSP is a particle tracing code that uses simulation particles to represent contaminant molecules or particulates. Instead of rays which instantaneously propagate from the source to the target element, CTSP concurrently advances positions of millions of simulation particles through a small time step Δt. Specifically, given a velocity $\vec{v}^{k+0.5}$, position of a particle is advanced from time step k to $k+1$ using $\vec{x}^{k+1} = \vec{x} + \vec{v}^{k+0.5}\Delta t$. Similar expression is used to advance the velocity due to acceleration. This approach is commonplace in rarefied gas dynamics Direct Simulation Monte Carlo (DSMC)[5] and plasma simulation Particle in Cell (PIC)[6] codes. The particle-stepping approach allows the code to incorporate external forces or inter-particle collisions. In the absence of these, the motion reduces to the straight line trajectory from the radiative heat ray tracing approach, since $d\vec{v}/dt = 0$ in the gas region. On surface impact, molecules reflect according to a specified reflection model which may be a function of temperature. A CTSP simulation thus concurrently captures the computation of the form factors between elements previously obtained from TSS, as well as the mass deposition rate from Equation 1. The step-wise approach for updating particle positions and the concurrent tracking of multiple particles also makes it possible to visualize volumetric macroscopic properties such as a contaminant plume density, stream velocity, and gas temperature. Such plots are not possible with the legacy approach since rays do not "exist" in the gas region between surface elements due to the instantaneous propagation.

Even in the "vacuum" of space, the number of physical atoms or molecules greatly exceeds computational and storage limitations of modern computers. CTSP, like other plasma and rarefied gas codes, uses a statistical approach in which each simulation particle represents a large number (billions) of real molecules. This ratio of real to simulation molecules is called a *macroparticle weight*, w_{mp} (also referred to as FNUM in DSMC codes). This approach assures that total mass, momentum, and energy of the system is retained while utilizing a much smaller, computationally feasible, number of molecules. The downside of this approach is that it introduces noise. As an example, let's assume that $w_{mp} = 10^{10}$. Each simulation molecule impacting a surface element is analogous to 10 billion real molecules making the impact. In regions without significant surface flux, we may end up with elements that are impacted by very few simulation particles. These elements will report large flux, while nearby surface triangles will have zero flux. The true deposition flux is given by the local average. In order to reduce this noise, PIC and DSMC codes are typically applied to steady-state problems in which the simulation results are collected, and averaged, over a large number of time steps. For statistically independent random variables, signal to noise ratios are akin to the mean divided by the distribution's standard deviation. Numerical noise thus scales as $1/\sqrt{N}$ where N is the number of simulation particles. Utilizing more particles (with each having a smaller w_{mp} weight) leads to a reduced noise, at the expense of a longer run time. As part of our analysis, we considered the effect of the number of particles and integration steps. The simulations presented here generally tracked around 10 million particles in the initial deployment stages. Simulations took around a week to complete utilizing a parallel architecture.

3. ANALYSIS INPUTS

Inputs used for the analysis are summarized in Table 1. A significant fraction of the modeling effort involved implementing loaders to ingest these data files.

Table 1. Listing of provided analysis inputs

Input	Format	Size
17 TSS geometry files covering distinct deployment phases	.tssgm	1.6 Gb
7 SINDA binary files providing element temperatures	.bin	13.4 Gb
2 .tssop optical property files	.tssop	<1 Mb
105 .nod and 9 .arr files containing material information	.nod/.arr	10 Mb
2 Tecplot files containing CSEA material assignments	.tec	88 Mb
Material fluxes from CSEA analysis report	.pdf	5 Mb
ISIM outgassing rates	.xlsx	8 Mb
Powerpoint slides listing timing of deployment phases	.pptx	4 Mb

3.1 Geometry

Of these inputs, the geometry loader required the most effort. As noted in the table, geometry was provided in the native TSS format. TSS is somewhat unique among general analysis tools in that it describes the model with assemblies of geometric primitives such as bricks, cylinders, cones, or discs. This is in contrast with the use of triangular and/or quadrilateral surface meshes in Finite Element Method (FEM) meshes. Each shape can be transformed through translation, rotation, or mirroring, with similar transformations also possible at the assembly level. These transformations can utilize mathematical expressions containing named variables. This generalized approach makes it possible for different deployment configurations to be represented by files identical except for the value assigned to a variable representing angular rotation of an appendage. The TSS model is typically built by the thermal engineering department by replicating, as much as possible, the mechanical Computer-Aided Design (CAD) drawings. Each TSS shape is assigned one or more thermal "node" IDs. These numbers, along with optional submodel names, are used by the SINDA thermal solver to relate the computed temperatures to the surface location. While CTSP already contained a rudimentary TSS loader developed in support of a prior project, the loader was not robust enough to handle all shapes and transformations of the provided geometry. Much of the initial analysis effort involved improving the loader, with the effort somewhat complicated by the lack of detailed documentation describing how surface transformations or mirroring are to be applied. Figure 1 visualizes the provided TSS files successfully loaded into CTSP, along with a time stamp indicating the beginning of each phase. The starts of phases 12 and 13 were not specifically provided to us and hence we placed them at uniformly spaced intervals between phases 11 and 14. Furthermore, the provided start time for Phase 10 (sunshield tensioning) did not match the information in the thermal solution. The start time was thus pushed out by about 10 hours to the timestamp at which the TSS node IDs corresponding to the deployed sunshield first appeared in the SINDA results.

3.2 Geometry Challenges

The use of analytical shapes makes it possible for TSS to capture conics exactly. CTSP, on the other hand, was developed as a general simulation program operating on a triangular and/or quadrilateral surface FEM meshes. During loading, the CTSP TSS loader tessellates the specified shapes into a collection of triangles and quadrangles. For this reason, some loss of surface detail is inherent whenever dealing with smooth conics. As an example, the top half of Figure 2(a) shows the base of the Deployable Telescope Assembly (DTA). The CTSP tessellation degenerates the smooth cylinders and discs into a collection of panels. The panels do not correctly line up since due to choices made in the creation of the TSS file, the conics were not rotated identically. In the case of the smooth conic used by TSS, the orientation is not relevant. However, in our case, it leads to panels that do not match up, leading to the presence of non-physical gaps.

Yet these gaps are not limited to degenerate conics. FEM meshes are built by specifying the position of vertices, and the vertex connectivity to build the cells. Since edges of adjacent cells share the same vertices, such a mesh is inherently watertight. This differs from what we have in TSS. TSS models are built by placing individual geometry primitives next to each other. Many surfaces that appear to be watertight actually contain small openings that become visible when the model is sufficiently zoomed in. One such an example is shown in the bottom half of Figure 2(a). Here we are looking at a section of the sunshield. The triangle highlighted in pink does not quite line up with the other nearby triangles, leading to an opening allowing molecules to enter. Similar such openings were also detected in the roof section of the Integrated Science Instrument Module (ISIM). These gaps, whether arising from CTSP's tessellation or from the mesh itself, can lead to non-physical molecular transport paths. Our geometry model captured only the outer surface (the skin) of the observatory. The internal cavities were not included. For instance, the entire ISIM is just an empty box. Molecules could enter ISIM through the gap in the roof, bounce around the cavity, make its way to the also-empty Aft Optics System (AOS) nose cone, and from there reach the primary mirror segments. This is clearly not a physical transport path, since these empty cavities do not exist in reality. In order to avoid such erroneous propagation, we proceeded to fill the internal spacecraft, Deployable Tower Assembly (DTA), AOS, and ISIM cavities with collector boxes, shown in red in Figure 2. These shapes were assigned a 100% sticking coefficient. The presence of these sinks prevents the non-physical transport path shown by the black line. By comparing the mass collected by the sinks, we found the mass loss to correspond to 0.1% of the total mass generated by sources. This small loss of mass conservation was deemed to be a viable alternative to otherwise having non-physical transport paths.
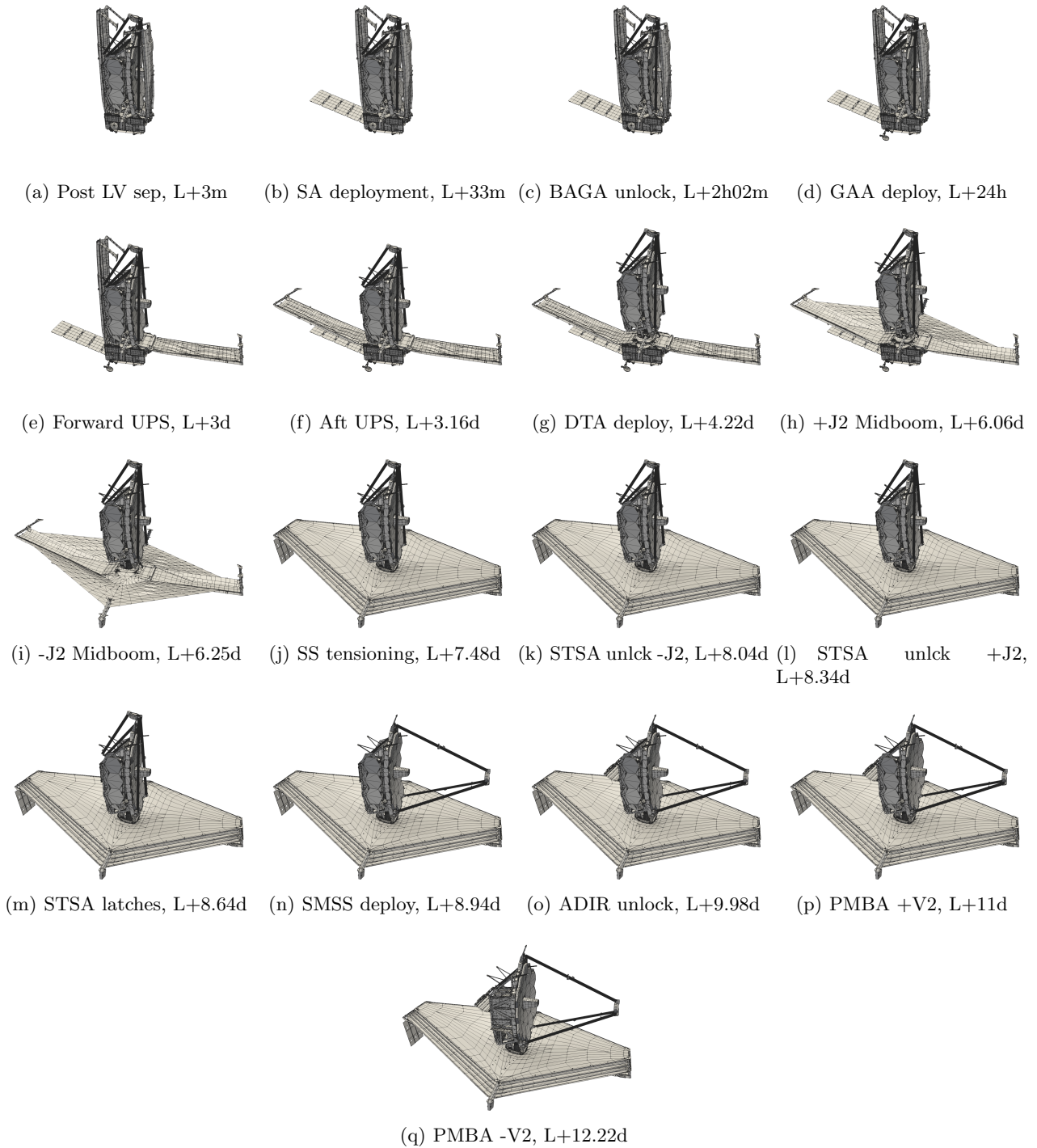
(a) Post LV sep, L+3m   (b) SA deployment, L+33m   (c) BAGA unlock, L+2h02m   (d) GAA deploy, L+24h

(e) Forward UPS, L+3d   (f) Aft UPS, L+3.16d   (g) DTA deploy, L+4.22d   (h) +J2 Midboom, L+6.06d

(i) -J2 Midboom, L+6.25d   (j) SS tensioning, L+7.48d   (k) STSA unlck -J2, L+8.04d   (l) STSA unlck +J2, L+8.34d

(m) STSA latches, L+8.64d   (n) SMSS deploy, L+8.94d   (o) ADIR unlock, L+9.98d   (p) PMBA +V2, L+11d

(q) PMBA -V2, L+12.22d

Figure 1. Geometry files capturing the deployment phases along with the utilized phase start time (UPS - upper pallet structure, L - launch, SS - sunshield, STSA - Sunshield Tensioning System Assembly, ADIR - Aft Deployable Infrared Radiator, PMBA - Primary Mirror Backplane Assembly).

(a) Lack of watertightness   (b) Internal sink objects
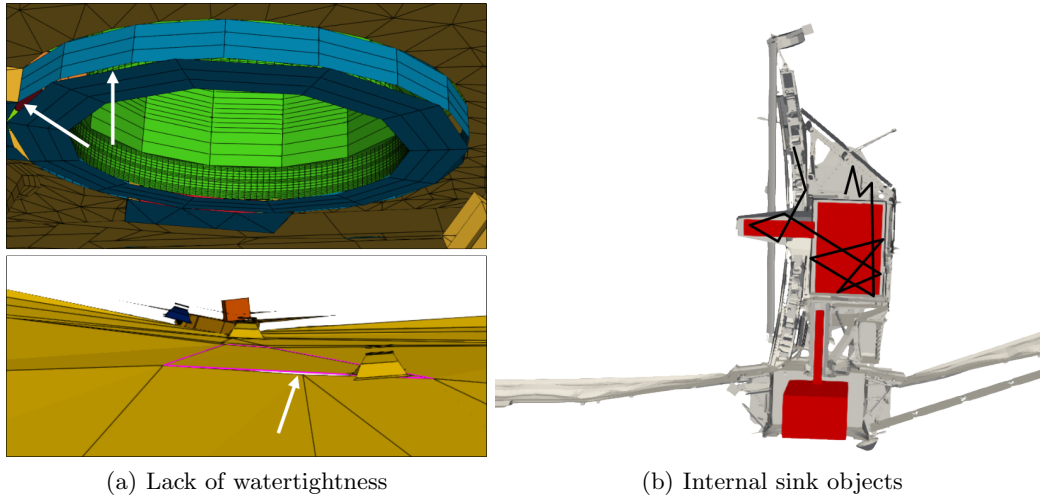
Figure 2. Visualization of typical tessellation issues leading to a lack of watertightness (left) and the inclusion of internal sink objects to prevent non-physical transport paths (right).

3.3 Material Assignment

The next major hurdle involved assigning surface materials. Water and molecular contaminant outgassing properties are specified at the material level. This requires that a material is specified for every surface element so that the appropriate outgassing model can be selected. The CSEA analysis utilized 18 material groups such as "multilayer insulation (MLI)", "single layer insulation (SLI)", "black thermal paint", and "Tiodize". Each shape specified within a TSS geometry file can be assigned a material, an optical property, and a color. Our initial hope was that one of these parameters will relate to the contamination material types used previously, but this was not the case. While all properties were assigned, the assignments appeared to be quite arbitrary. Per discussion with the thermal team, we found that the TSS properties are indeed unused by the thermal solver, and are instead obtained from additional ".nod" and ".arr" files. We were subsequently provided these files and wrote a parser to generate a map of material types for each node ID. However, by comparing the resulting assignment, it quickly became obvious that the extracted data was insufficient. The thermal inputs specified only the outermost material. There was no distinction made between MLI, SLI, or a composite wrapped by MLI, with all such surfaces assigned to a Kapton group. From the contamination standpoint, a composite covered by blanketing will have very different outgassing properties than a single sheet of an SLI film.

Therefore, the next step, which was also among the most time consuming aspects of the entire analysis, involved manually adjusting material types for clearly mislabeled nodes with the help of material assignment pictures in the CSEA analysis. This work involved utilizing a Python script to generate a lookup table output file mapping TSS node ID to a material type from user-specified element ranges. Eventually we were able to obtain a copy of a Tecplot file containing the CSEA material assignment. The final division is visualized in Figure 3. Different colors correspond to different materials.

3.4 SINDA Temperatures

The temporal evolution of surface temperatures was obtained from 7 SINDA output files totaling approximately 13 Gb. These files use Fortran binary format to store tabular data, with the first row specifying the node IDs, followed by an arbitrary number of additional frames. Each frame lists the time point followed by temperatures for all nodes. A parser was written to load the files while downsampling the resolution to 100 s increments to reduce the memory footprint. Linear interpolation is used for the intermediate values. Figure 4 illustrates temperature variation for several arbitrarily selected elements (nodes). Note that time on the horizontal axis is plotted on a log scale. The yellow-white shading indicates different deployment phases. We can see general cooling, although there are exceptions. The green trace corresponds to a sun-facing element on the spacecraft. The trace shown by the purple line is an element on the outer side of the forward UPS. While this element cools

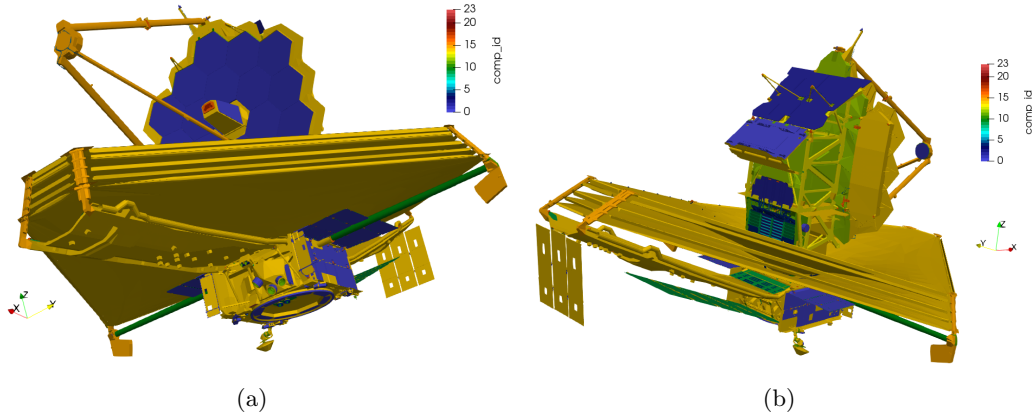(a)   (b)
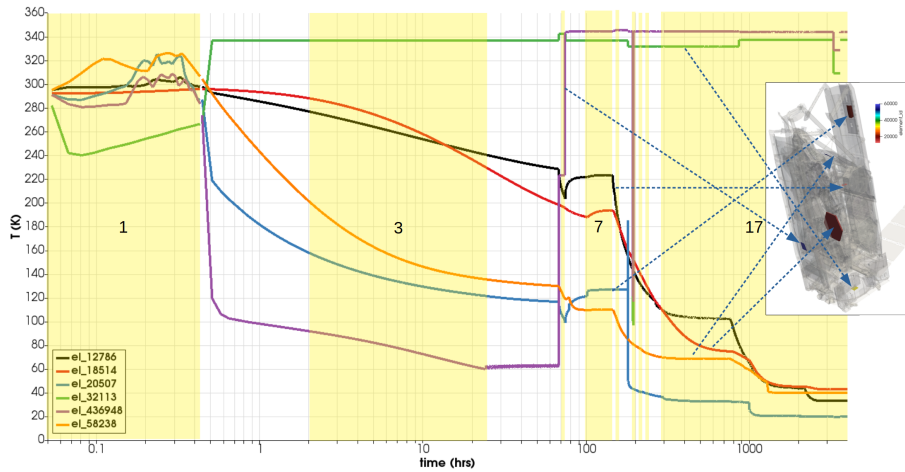
Figure 3. Visualization of material assignment.

Figure 4. Temperature variation for several thermal nodes. The yellow/white shading delineates deployment phases.

over the first 4 phases, its temperature rapidly increases in phase 5 (starting approximately 72 hours, or 3 days, post launch vehicle separation). This change in temperature is due to the pallet being lowered into a sun-facing orientation. Any ice that may have accumulated over the prior 72 hours can now be expected to desorb.

3.5 Continuity

As will be discussed below in Section 4.3, we divided the 180 day period of interest into 200 integration steps spanning the 17 geometry files described in Section 3.1. Some of these steps involved advancing to the new deployment configuration. Here we used a restart file to save to a disc the amounts of water and VCM molecules accumulated on each surface element. Data was stored according to the TSS node and subdivision id, as well as the front or back side. This subdivision allowed us to target a specific surface triangle or a quad arising from CTSP's tessellation of conics. The side information allowed us to distinguish material collected on the two sides of thin plates. In order to avoid an artificial mass loss, it is important to retain continuity in surface elements between deployment phases. In other words, every item stored in the restart file needs to map to some surface element in the subsequent stage. We noticed two primary transition events when this was not the case. First, as depicted in Figure 5(a), the sunshield cover is removed after Phase 7. Physically, the cover is rolled up into two cylinders that are stored on the sun facing side of the pallets. These rolls were included in the TSS files, but not until Phase 10. Also, there was no agreement in node IDs between the membrane cover elements and these rolled up structures. As such, we isolated the geometrical primitives of these rolled up covers from the Phase 10 TSS file and incorporated them into Phase 8 and 9 geometries. We also modified the restart subroutine to distribute mass from the original range of node IDs corresponding to the sunshield cover to the new range corresponding

(a) Membrane covers, Phase 7

(b) Cover rolls added to Phases 8-9

(c) Missing membrane over pallets

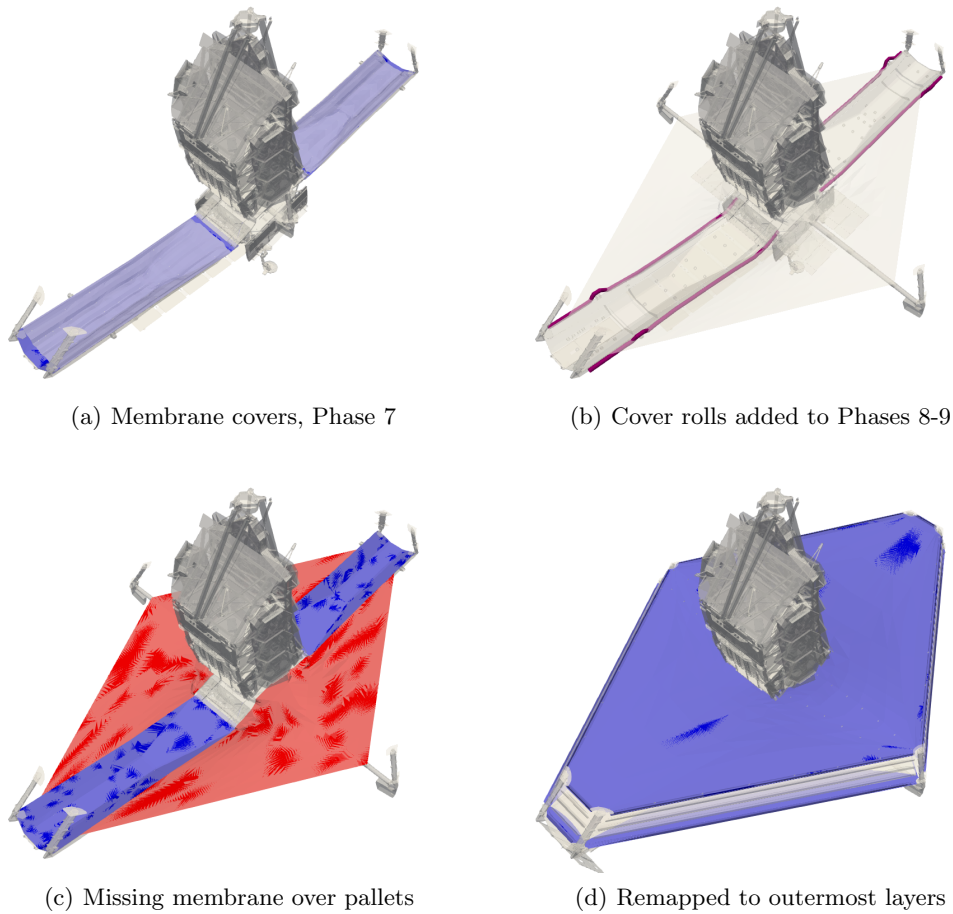(d) Remapped to outermost layers

Figure 5. Mapping of surface elements to retain mass conservation.

to the rolled up covers present in the subsequent geometry file.

Similar discontinuity was also observed between the partially-deployed (Phase 9) and the fully deployed (Phase 10) sunshield, Figure 5(c). Furthermore, Phases 8 and 9 do not include a sunshield membrane over the pallet. Here we again included a node-id range-based remapping of mass. Due to this mapping, the locality of deposition during Phases 8 and 9 is discarded and the accumulated ice distributes evenly over the sunhield. This averaging introduced negligible error on the final ice buildup since the accumulation during these two phases is limited by both the relatively short duration (about a day combined) and a warm surface temperature (+200K).

4. NUMERICAL IMPLEMENTATION

4.1 Particle Generation and Transport

As noted earlier, CTSP uses simulation particles to represent real molecules. Each simulation particle corresponds to some (typically around 10^9) w_{mp} number of real molecules. This weight can either be uniform for all particles of a species or can be individually varying. Here we had to utilize a variable weight approach due to the large variation in outgassing rates over the considered analysis time period. The input files specified the desired macroparticle surface density (the number of macroparticles per m^2). The total number of *real* molecules generated in a time step Δt on an element with surface area A due to mass flux Γ is

$$N_{real} = (\Gamma/m)A\Delta t \tag{3}$$

where m is the mass of a single molecule. The desired number of simulation particles is obtained per

$$N_{sim,target} = \text{np\_den} \cdot A \tag{4}$$

where np_den is the user-specified macroparticle surface density. The macroparticle weight is thus

$$w_{mp} = N_{real}/N_{sim,target} \tag{5}$$

On low-outgassing surfaces, the resulting weight would lead to tiny fractional particles that have a negligible impact on deposition while still taking up computational resources. Therefore, we also utilize a minimum $w_{p,min}$ value to prevent the creation of such tiny samples. This floor is set such that a particle of $w_{mp,min}$ contributes approximately 0.001 A deposition on a typical surface element on impact. The actual integer number of simulation particles to be created is computed per

$$N_{sim,sample} = \text{int}(N_{real}/w_{mp} + \mathcal{R}) \tag{6}$$

where $\mathcal{R}$ is a random number. This sampling approach is typical of stochastic particle simulations. The random value, coupled with the "floor" operation associated with conversion of a real number to an integer leads to the simulation producing the desired fraction value on average. This stochastic approach is commonly found in PIC or DSMC simulations.

The generated particles are advanced through small simulation time steps by integrating the equations of motion

$$\frac{d\vec{x}}{dt} = \vec{v}$$
$$\frac{d\vec{v}}{dt} = \vec{F}_{tot}/m$$

using the Leapfrog method. It should be noted that in this case, $F_{tot} = 0$ and as such, particles move in straight lines. Optionally, inter-molecular collisions could be included via the DSMC method, however this was not the case in the considered simulation. Contaminant vapor densities rapidly decay such that intermolecular collisions are negligible.

4.2 Surface Adsorption

At each time step, the code checks for surface impact by performing line-triangle intersection checks. Whenever a particle hits a surface, the code needs to determine if the molecules represented by the macroparticles stick to the surface or whether they desorb immediately. Historically, we have used activation energy and surface temperature to compute molecular residence time, which was compared to the simulation time step size. This approach is however not applicable to modeling water vapor deposition. A new model was developed based on the Murphy-Koop partial pressure equation.[7] The algorithm is as follows:

At the beginning of each time step, we compute water vapor evaporation "capacity" for each surface element. This capacity is the number of molecules that would desorb from an infinitely large reservoir at the element temperature in a given time step. We start by computing water vapor partial pressure per,

$$P = \exp\left(9.550426 - \frac{5723.265}{T_{el}} + 3.53068\ln(T_{el}) - 0.00728332T_{el}\right) \tag{7}$$

we next use the "Langmuir flux" relationship to set the surface outgassing flux,

$$\Gamma = \frac{\alpha P}{\sqrt{2\pi m_{water}k_B T_{el}}}, \qquad \alpha = 1.0 \tag{8}$$

The corresponding number of molecules leaving is thus

$$N_{cap} = \Gamma A_{el}\Delta t \tag{9}$$

(a) Rotation with orthogonal projection   (b) Selected Sun facing element
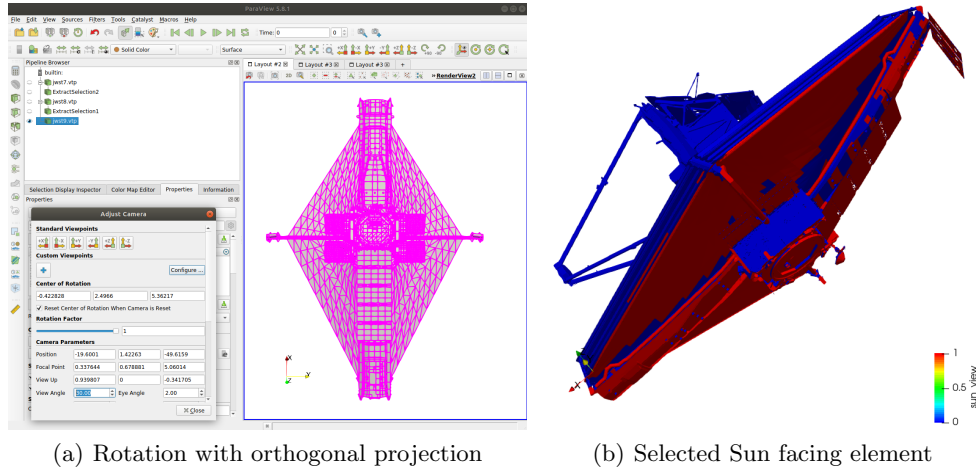
Figure 6. Process for flagging sun-facing elements.

Whenever a molecule hits a surface, we reduce N_{cap} by the impinging w_{mp}. As long as the capacity remains positive (implying that the incoming flux has not exceeded the anticipated outgoing flux), the molecule is bounced off using the Lambertian model, and the capacity is reduced. Otherwise, the molecule is captured by incrementing a counter of adsorbed molecular count on the surface element. Here we also account for the possibility of only a fractional macroparticle reflecting. The number of molecules N adsorbed to each surface element of area A is eventually used to compute the deposition thickness. We treat molecules as a uniform film with height

$$h = (4\pi r^3 N)/(3A) \qquad , r_{water} = 3.103 \times 10^{-10} \text{ m} \tag{10}$$

The utilized value of r_{water} produces 1 Å of deposition given 10^{-7} kg/m^2 surface mass density, as specified in MIL-STD-1246C. While solid ice density could be used instead, we utilized this scaling for consistency with the standard.

A different approach was used for the VCM deposition. As the details of VCM adsorptions were not discussed in the CSEA analysis, we implemented a model based on a temperature varying sticking coefficient. The sticking fraction followed the following relationship: 100% at -60 °C, 50% at -40 °C, 25% at -25 °C, 10% at 0 °C, 0.01% at 10 °C, and 0% at >10 °C. In addition, 10% of impinging VCM was assumed to stick *permanently* on sun-facing surfaces warmer than 10 °C to model photopolymerization.[8] This last item required us to identify the sun-facing elements. These elements were flagged by utilizing Paraview (program for visualizing scientific data). For each of the 17 configurations, the spacecraft was oriented such that the solar panel was parallel to the screen. Switching to orthogonal projection, we then used the mouse box selection to highlight all elements. Since Paraview selects only nodes visible in the current view, this selection produced only the elements with a view to the sun. The node IDs were saved to a file and a parser was written to read them in. This process is illustrated in Figure 6.

4.3 Time Marching

Historically, CTSP was used mainly to compute steady-state deposition rate starting with an initially clean spacecraft. We were now interested in computing the redistribution over a long time period (180 days) while considering multiple geometry configurations and temperatures. Due to the need to push individual particles, the CTSP simulation time step is limited by the molecular speed to relatively low values such as 10^{-4} s. Using such a small time step, it is simply not feasible to simulate the entire 180 day time period in a reasonable time. Therefore, the entire deployment sequence was captured with a sequence of short steps, with each step used to calculate the net deposition rate $\dot{N}$ over the step interval. The overall algorithm is as follows:

1. Given an integration step from t_1 to t_2, set current time to $t_{mid} = 0.5(t_1 + t_2)$.

2. Assign surface temperatures based on t_{mid}.

3. Desorb any previously accumulated water by looping through all surface elements, and on each computing the total desorption over $\Delta t_{step} = t_2 - t_1$ up to $\min(N_{cap}, N_{actual})$ molecules.

4. Allow these molecules to redistribute (stick to other surfaces) or leave the computational domain by running for a sufficient number of time steps (typically 1000).

5. Record initial molecular counts on each surface element, N_i.

6. Run for n (5000 in the nominal cases) Δt time steps, during which we continuously sample new molecules from sources.

7. Compute molecular deposition rate on each element per $\dot{N} = (N_f - N_i)/(n \Delta t)$ where N_f is the final number of surface molecules

8. Integrate surface molecular count per $N^{k+1} = N^k + \dot{N} * \Delta t_{step}$.

During testing with a simplified parallel plate geometry, we found that this approach both produces an excellent agreement with the direct integration of Equation 1 used with an analytical view factor as long as small integration steps are used initially to resolve the high outgassing shortly after launch. We thus used a front-loaded approach for the JWST analysis. The integration sequence is summarized in Table 2. We can see that out of the 200 total steps spanning a 180 day interval, over one quarter (58) are used to simulate the first three days. In order to characterize sensitivity of the actual JWST analysis on the integration step size, we also compared results to a setup with only 100 steps. These results are visualized in Figure 7. A good agreement can be seen, with the coarse case leading to a slight over-prediction of the contaminant thickness. This is mainly visible on the forward pallet. This overprediction is due to the use of a larger integration step in the step 8 above.

4.4 Simulation Input Files

CTSP is a command-line code that uses a script file to drive the simulation. The input file can include additional script files, and can also utilize mathematical expressions with variables. We used a Python script to generate the entire simulation sequence automatically. The listing below shows a typical input file. This particular file is for Sequence 10, with mapping specified to distribute mass on the partially deployed sunshield to the top and bottom surface of the top and bottom layers.

Phase	Number of Steps	Step Size (hours)
1	4	0.12
2	10	0.15
3	20	1.1
4	24	2
5	4	1.3
6	20	1.3
7	20	2.2
8	2	2.3
9	8	3.7
10	10	1.3
11	4	1.8
12	4	1.8
13	4	1.8
14	10	2.5
15	6	4.1
16	10	2.9
17	40	100

Table 2. Time marching discretization.

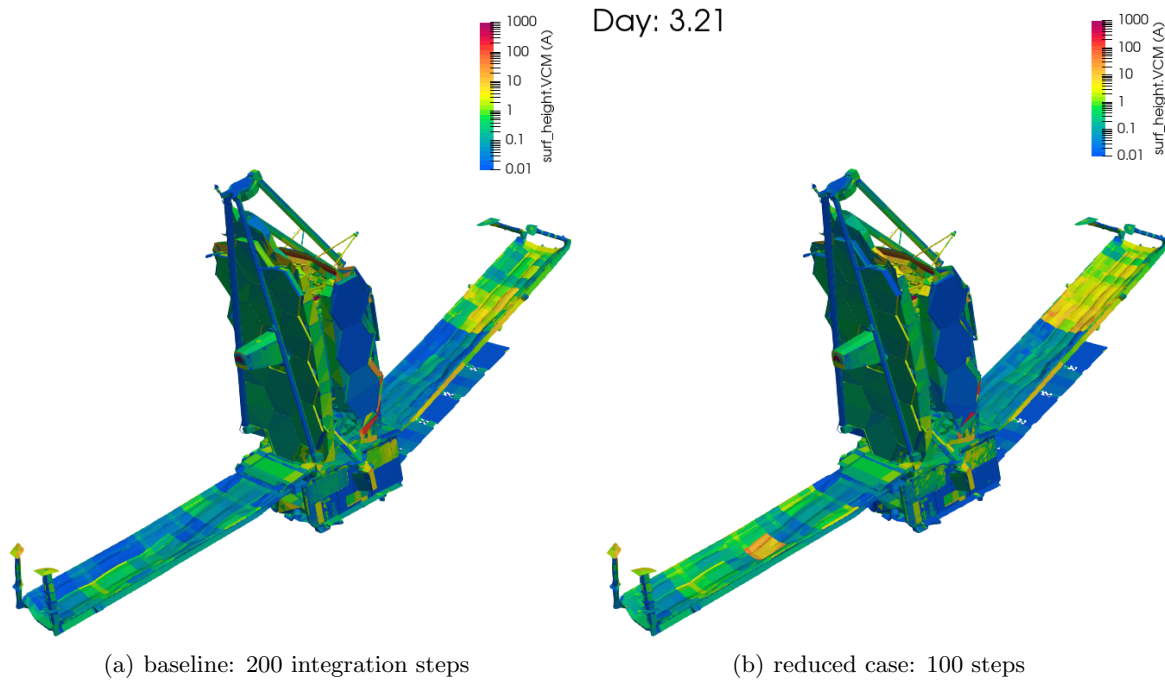(a) baseline: 200 integration steps   (b) reduced case: 100 steps

Figure 7. Sensitivity study considering the number of integration steps. Data is plotted on a log scale.

```
#JWST simulation sequence 10
set_variable{name:stage, value:10}
include{file_name:inputs/ctsp-mats.in}
surface_load_TSS{file_name:tss/jwst10.tssgm, group_by:element, mapping:[
  JWST_Thermal_Files/node_mat_mapping.csv,1],sun_view_file:tss/sun_view10.csv}
surface_load_TSS{file_name:tss/vent_covers2.tssgm, group_by:element, mapping:[
  JWST_Thermal_Files/node_mat_mapping.csv,1]}
surface_load_TSS{file_name:tss/trap2.tssgm, group_by:element, mapping:[
  JWST_Thermal_Files/node_mat_mapping.csv,1]}
surface_load_TSS{file_name:tss/harness_vent.tssgm, group_by:element, mapping:[
  JWST_Thermal_Files/node_mat_mapping.csv,1]}
volume_mesh{dx:0.1,dy:0.1,dz:0.1,expand:[1 1 1 1 2 1]}
surface_props{comps:*, mats:none, c_stick:-1.0, temp:10}
surface_props{comps:/vent_.*/, mats:vent, c_stick:1.0, temp:270}
surface_props{comps:trap, mats:none, c_stick:1.0}
# temperature profile
load_temperature{file_name:temps/LA13B_v5.5t18d-C_PH2a-3d_Ts.bin,dt:100}
load_temperature{file_name:temps/LA13B_v5.5t18d-C_PH3d-D30_Ts.bin,dt:100}
restart_load{file_name:restart/restart09,load_particles:false,map1:[out/400000/401000/in/
  25100/25700],map2:[in/24100/24600/in/25100/25700],map3:[in/22100/22320/in/25100/25700],
  map1:[in/400000/401000/out/25100/25700]}

# **** STEP 0 ****
world{set_time:617674}
set_variable{name:step,value:0}
set_variable{name: dt_integrate, value: 1.711e+04}
include{file_name:inputs/ctsp-master.in}
```

```
# **** STEP 1 ****
world{set_time:634781}
set_variable{name:step,value:1}
set_variable{name: dt_integrate, value: 1.711e+04}
include{file_name:inputs/ctsp-master.in}

# **** STEP 2 ****
world{set_time:651888}
set_variable{name:step,value:2}
set_variable{name: dt_integrate, value: 1.711e+04}
include{file_name:inputs/ctsp-master.in}

# **** STEP 3 ****
...

# **** STEP 4 ****
...

# post process
include{file_name:inputs/ctsp-finish.in}
```

The `ctsp-mats.in` file lists some common options and also specifies material data

```
options{log_level:info,randomize:true,delete_back_side:true, screen_diag_freq:10,
  num_threads:2}
world{sun_direction:[-0.34202, 0, -0.939693]}
#specify materials
solid_mat{name:none, weight: 100}
solid_mat{name:mli, weight: 100}
solid_mat{name:vent, weight: 100}

# water radius to produce 1 angstrom at 0.01mu*g/cm^2 surface density per Trible Table 2-3
molecular_mat{name:water, weight: 18, mp_density:5, mpw_min:5e14,r:1.9252e-10,
  desorption_model:murphy_koop}

#50% stick at -40C, 25% stick at -20C, 10% at 0C, LB added 100% at -60C
#using same radius as water, using 60second desorption time interval
molecular_mat{name:vcm, weight: 54, mp_density:50, mpw_min:5e11,r:1.9252e-10,
  c_stick:[1.0@213, 0.5@233, 0.25@248, 0.1@273, 0.01@283, 0@284],
  c_stick_perm:[0@0,0@273,0.1@274],sun_view_only:true,
  desorption_model:c_stick, time_constant:0.2}
```

The `ctsp-master.in` file controls the actual execution of each simulation,

```
#delete existing sources
sources_clear{}

#sources
source_cosine_jwst{comps:*, mat:water,v_drift:100,flux_file:inputs/mw_rates.csv,
  start_ts:2000}
source_desorption{dt_integrate:$dt_integrate$}
```

```
particle_trace{file_name:trace$stage$,mat:water,num_traces:1000, max_id:10000, skip:100}
run_sim{dt:1e-4, num_ts:5000, log_skip:20, ts_steady_state:2000, ts_clear_particles:2000}

# scale results
scale_outgassing{mats:water, model:const, dt:$dt_integrate$}

surface_save_vtk{file_name:jwst$stage$-$step$,vars:[temperature, surf_height.water]}
volume_save_vtk{file_name:field$stage$-$step$,vars:[nd.water]}
```

The `ctsp-finish.in` performs close up activities, such as saving the restart data,

```
restart_save{file_name:restart/restart$stage$,group_elements:true,save_particles:false}
volume_save_vtk{file_name:"field$stage$",vars:[nd.water]}
surface_save_vtk{file_name:"jwst$stage$",vars:[temperature,
  surf_height.water, stuck_surf_height.water]}
```

Simulations were run on a Linux workstation featuring a 10 core 3.2 GHz Intel Xeon processor and 64 Gb of RAM. CTSP supports multiprocessing by essentially concurrently running multiple serial simulations and averaging the individual results. This is analogous to splitting up the total particle population across multiple CPUs. The entire 200 step sequence took almost two weeks to complete, however the majority of the computational effort was spent in simulating the first six days post launch. In these initial phases characterized by high outgassing rates, the simulation typically tracked about 10 million particles per time step.

5. CONTAMINANT SOURCES

5.1 Flux Temperature Dependence

Molecular outgassing arises from molecules "trapped" inside the material diffusing to the surface by random motion, and then desorbing to the gas phase. In addition, the surface may already contain some chemical film, such as water or lubricants. Computing the outgassing rate requires solving the diffusion equation for a particular material shape and composition, which is numerically prohibitive. Therefore, it customary to use tests such as ASTM-E-1559 to experimentally measure the outgassing rate (or flux) of different materials at temperatures of interest. The sample is heated to a specified temperature and QCMs (quartz crystal microbalances) set to different collection temperatures measure the deposition. The use of multiple QCMs allows the contamination engineer to separate water vapor, which only collects on cryogenic surfaces, from volatile condensable materials. Such outgassing characterization tests were performed for JWST materials, although the actual raw data was not available to us in the performance of this analysis. Instead, we utilized analytical fits to the raw data reported in [1]. Outgassing rates tend to demonstrate two distinct phases. First, there is the initial high rate of mass loss arising from surface desorption. Subsequently, the rate diminishes as the mass production becomes dominated by material diffusion. The outgassing flux models were generally given in the form $\Gamma(t,T) = \Gamma_1(t,T) + \Gamma_2(t,T)$. These terms correspond to the short- and the long- term decay.

While these expressions simplify the analysis, they are not mass conserving. Assuming the temperature increase is not so excessive as to introduce chemical decomposition, higher surface temperature leads to an increase in the material diffusion rate, however the total amount of mass loss (obtained by integrating to infinity) remains constant,

$$\Delta m \equiv \int_{t=0}^{\infty} \Gamma(t,T)dt = C \tag{11}$$

In other words, we should expect that Δm is constant regardless of the temperature T. The desorption curves should then change as shown in Figure 8(a). If green curve is the nominal behavior, a decrease in surface temperature should spread out the outgassing flux over a longer time interval, as qualitatively shown by the blue line. A warmer temperature on the other hand should concentrate the primary mass loss to a smaller time window. However, for several materials, the models specified in the CSEA produced plots as shown by the purple line. We found the SLI model to be especially problematic. A 200 K change in temperature led to almost 4

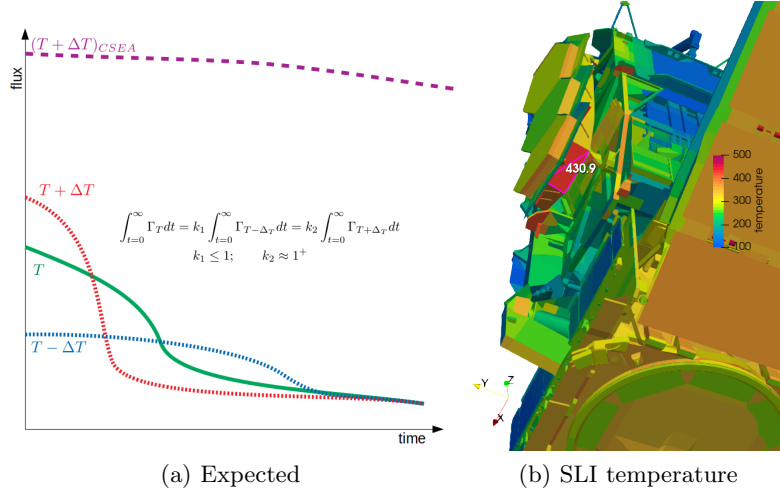(a) Expected   (b) SLI temperature

Figure 8. (a) Expected and actual flux variation with temperature, (b) illustration of hot elements.

orders of magnitude change in total mass loss. This did not seem physically reasonable, especially considering we are dealing with a thin layer of metallized polymeric film. Such a wide range of temperature was frequently encountered due to SLI rapidly warming up or cooling according to the sun illumination. As an example, the backplane of the folded primary mirror, shown in Figure 8(b) was calculated to remain at >430 K for 5.5 days. During this period, the SLI outgassing model predict the total outgassed mass to exceed the expected mass of the film, which is not realistic.

Therefore, for this analysis, we implemented flux corrections to retain mass conservation, as much as possible. VCM flux equations were generally modified to the following form,

$$\tau \sim k_2 \exp\left(\frac{E}{T} - \frac{E}{T_0}\right)$$

$$\Gamma \sim k_1 \exp\left(-t/\tau\right) \quad \longrightarrow \quad (k_1/k_2)\exp(-k_1 t/\tau)$$

where E is a fitting coefficient. Water models were not as strongly affected by temperature as VCM, and also due to a different functional form, were not so easy to modify. For water, we mainly limited the maximum temperature at which the models were evaluated.

These outgassing fluxes were implemented in CTSP within a custom `source_jwst` material injection source. This source is attached to all surface elements and is called at every time step. The source uses the element's specified material type to select the appropriate flux equation. Flux is then scaled by the time step and the element area to determine the number of real molecules injected within the integration time step. The specified macroparticle surface density is then used to calculate the number of simulation particles of a variable macroparticle weight. These particles are launched from random positions on the element. Initial velocity direction is also randomly sampled utilizing the cosine law about the surface normal.

Another important source of contaminant production are spacecraft vents. The vents used in our analysis are shown in Figure 9. Specifically, there are 5 vents located on the spacecraft. Wire harnesses are vented from two vents at the base of the core region. Here we also find a vent for the deployable tower assembly, or DTA. The ISIM instrument module contains three vents in the attic section, as well as two additional IEC vents near the sunshield. Finally, the optical system is vented through the forward face of the AOS "nose cone" covering the tertiary mirror. Rates for these surfaces were derived by the project contamination control team based on historical data, the mass of the vented components, and vacuum chamber measurements, where available.
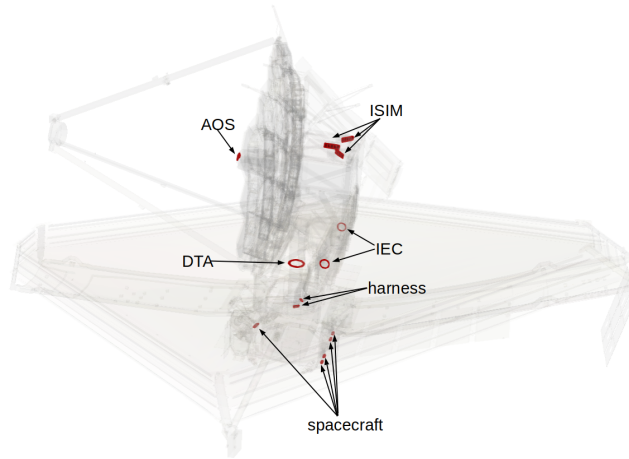
Figure 9. Vent locations.

6. RESULTS

6.1 Water Ice

In this section we present a high-level overview of the computed results. Numerous additional plots were generated in support of project requests. Examples of these additional plots included the water ice thickness on hinges prior to deployments, the impact of hypothetical leak paths on mass transport, and the impact of secondary mirror inboard hinge motor heating. The plots in Figure 10 show water ice deposition thickness at 9 distinct time points selected from the overall 200-step integration sequence described on Page 11. The evolution of surface temperature corresponding to these plots is shown in Figure 11. We can observe that initially, water is concentrated on the exposed faces of the sunshield membrane unitized pallets structures (UPS). These surfaces are covered in blanketing which cools rapidly due to the spacecraft orientation. The primary and secondary mirrors cool at a slow rate and thus initially do not collect any water. Around day 3, first the forward, and then the aft UPS are lowered, see Figure 1. While not visible in the view shown in Figure 11, this lowering leads to a warm up of the bottom side of the pallet. The previously collected ice quickly sublimates, leading to a temporary localized increase in water vapor partial pressure. The majority of this water flies off to space as it is released on the sun-facing spacecraft side.

In Figure 10(d) we see the state after the initial sunshield deployment but prior to tensioning. The specks on the membrane may be arising from numerical noise, but it is also possible that this could be a numerical artifact arising from a node number re-use. In other words, it is possible that the node IDs assigned to these elements actually corresponded to a different surface in the prior stage. This discrepancy should be investigated in more detail, but given the short duration of this particular stage, it did not seem to warrant the effort. Figure 10(e) then shows the water concentration shortly after sunshield tensioning is complete. One important feature to notice is that we do not see any significant increase in icing on the mirror segments, which was the primary contamination concern. As can be seen in Figure 11(e), mirror segments remain relatively warm at $T \sim 170$ K. The Murphy-Koop model does not predict significant icing until about 150 K. Figure 10(f) illustrates the configuration shortly after the secondary mirror deployment. This deployment was of particular concern, since the inboard hinge that had to be heated prior to deployment had a direct line of sight to the mirror. The concern here was that subliminating ice would collect on the mirror. The thermal prediction suggested that the secondary mirror was still relatively warm to prevent any icing. However, even in the conservative case of a cryogenic mirror, our analysis indicated a tolerable amount of icing assuming a full release of water already collected on the motor housing. Figure 10(g) then shows the state right prior to the $+J2$ primary mirror segment deployment. Comparing Figures 10(h) and 10(i) we can see very little additional icing on the mirror segments over the remaining 160 day span. The only noticeable increase in surface deposition is on the aft section of the sunshield. This icing arises from water released by the IEC vents and continued outgassing from the core region. The resulting thickness of icing on the sunshield covers was not an item of concern for the thermal team.
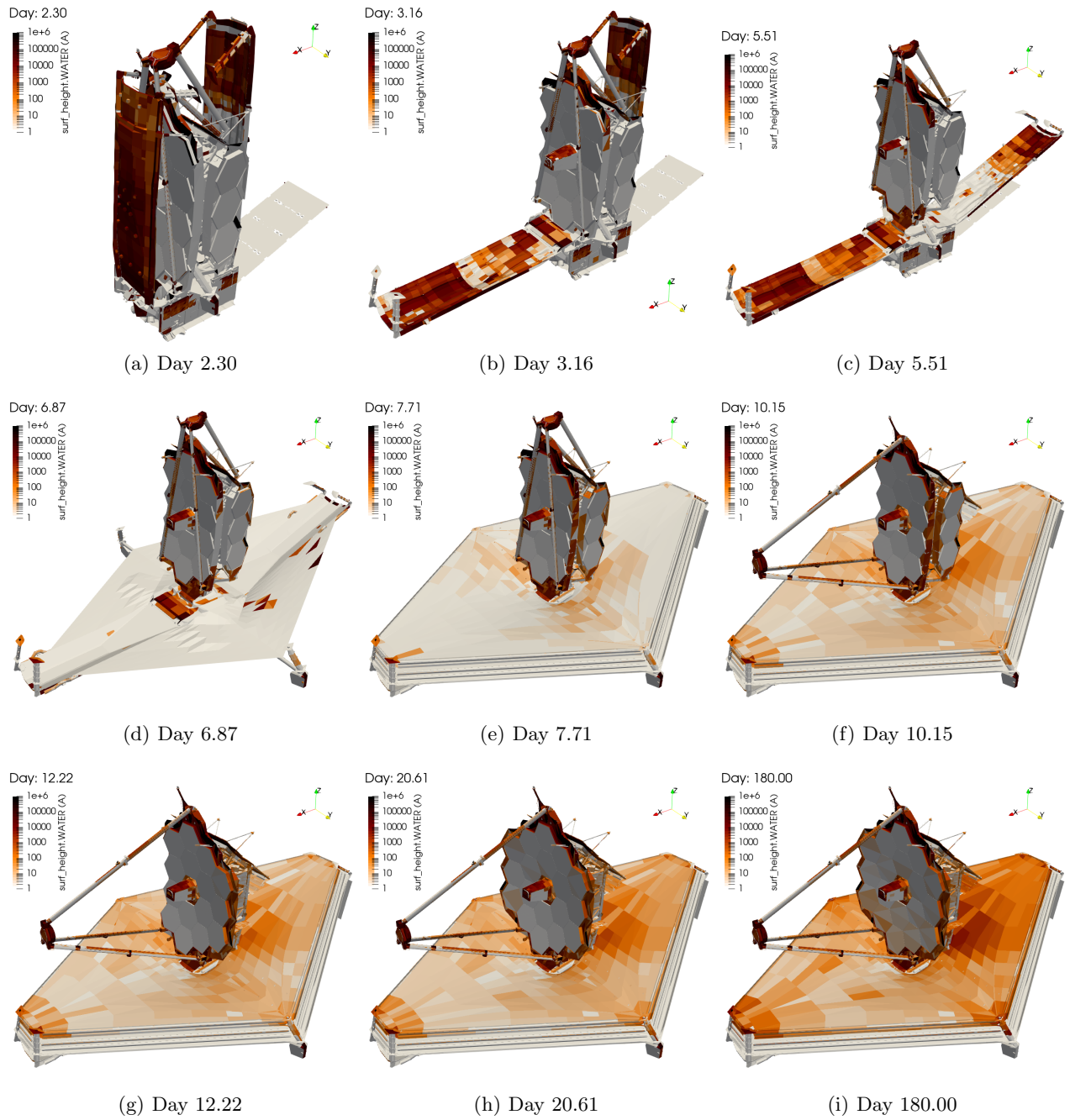
(a) Day 2.30   (b) Day 3.16   (c) Day 5.51

(d) Day 6.87   (e) Day 7.71   (f) Day 10.15

(g) Day 12.22   (h) Day 20.61   (i) Day 180.00

Figure 10. Progression of water ice surface deposition thickness.

(a) Day 2.30   (b) Day 3.16   (c) Day 5.51

(d) Day 6.87   (e) Day 7.71   (f) Day 10.15

(g) Day 12.22   (h) Day 20.61   (i) Day 180.00
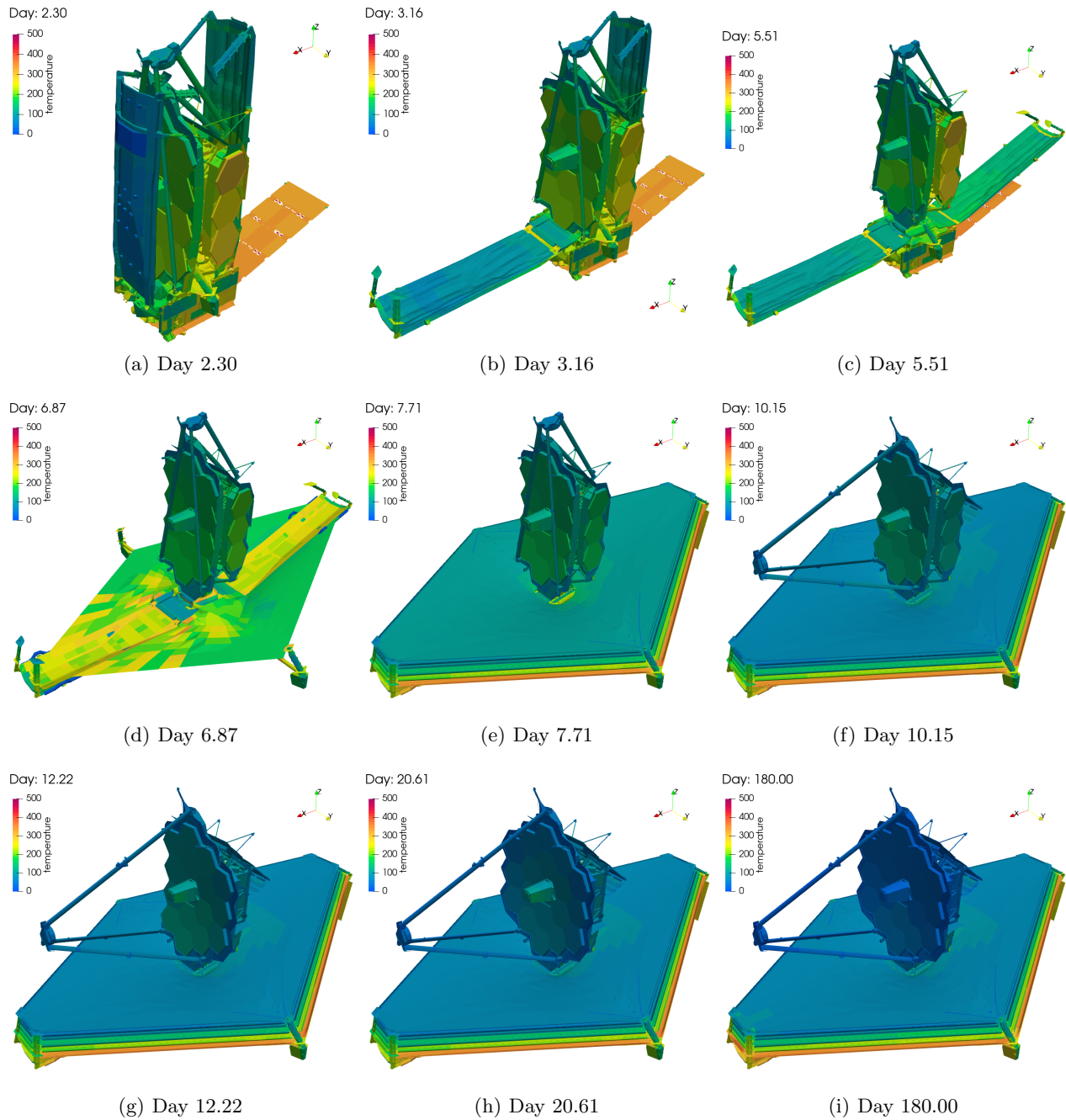
Figure 11. Temperature variation corresponding to the water deposition from Figure 10.

(a) Water concentration   (b) Temperature
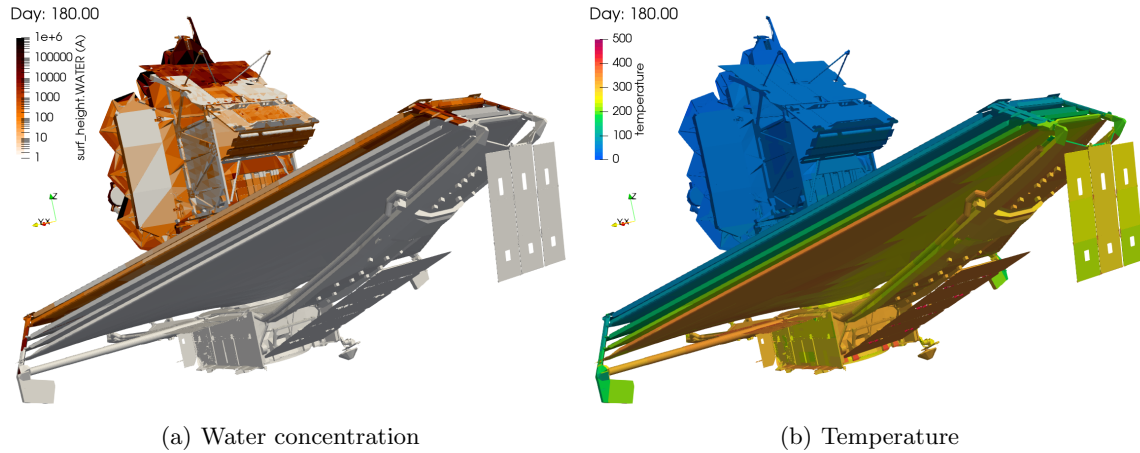
Figure 12. Another view of water concentration after 180 days.

(a) Day 0.18   (b) Day 3.06
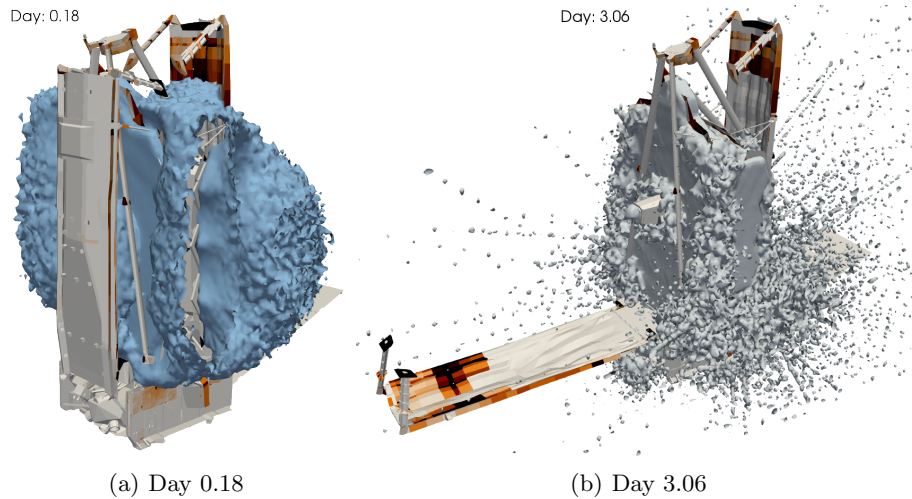
Figure 13. Visualization of water plume density at two different time points. Plot in (a) corresponds to stage 1, plot in (b) corresponds to stage 5.

Figure 12 illustrates the water deposition from an angle exposing the spacecraft and the observatory aft sides. An important observation to make here is that no water is found on the warm sun-facing spacecraft side. The highest concentration of ice is observed on the top section of the ISIM radiator and on the back "skirt" of the central primary mirror segment.

Figure 13 visualizes water vapor concentration at two different time points. The ability to compute contaminant density plots is one of the strengths of the particle-based approach implemented in CTSP as it allows us to better understand the propagation of the contaminant. As can be seen from the first plot, water is initially concentrated in the enclosed space between ISIM and the stowed pallets. One of the primary sources here are the packed sunshield membranes. Given the initial stowed configuration, these water molecules bounce between the central mirror segment and the forward pallet. On the aft side, similar behavior is seen with the molecules trapped between the back side of the ISIM module and the aft UPS. Eventually the molecules reach the outer edge and diffuse primarily in the $\pm$ J2 direction. By day 3.06, the water vapor concentration has decreased, as indicated by the lighter shading of the isosurface. Now a more noticeable source of water becomes the IEC vent and the core region, although we continue to see material outgassing in the vicinity of the primary mirror segments.
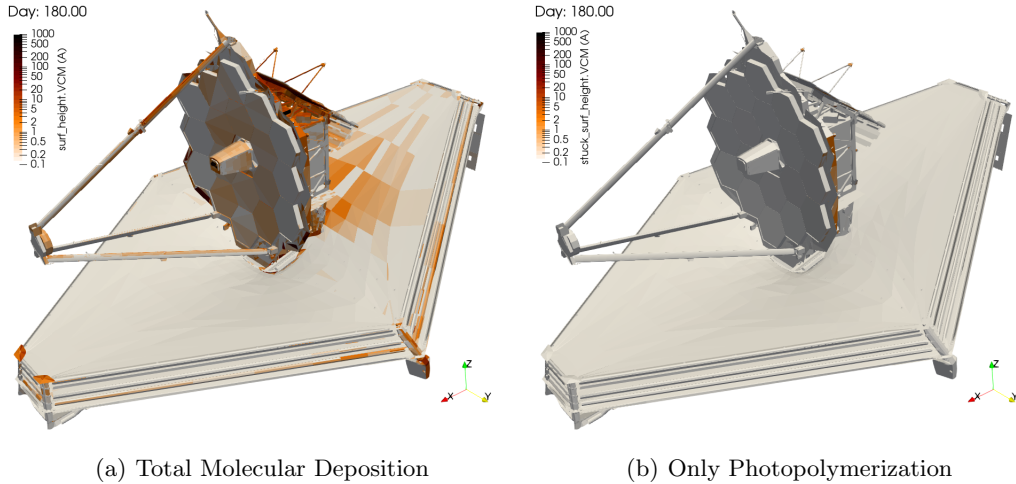
(a) Total Molecular Deposition   (b) Only Photopolymerization

Figure 14. Molecular contaminant deposition thickness after 180 days. These plots correspond to the end of stage 17.

(a) Total Molecular Deposition   (b) Only Photopolymerization
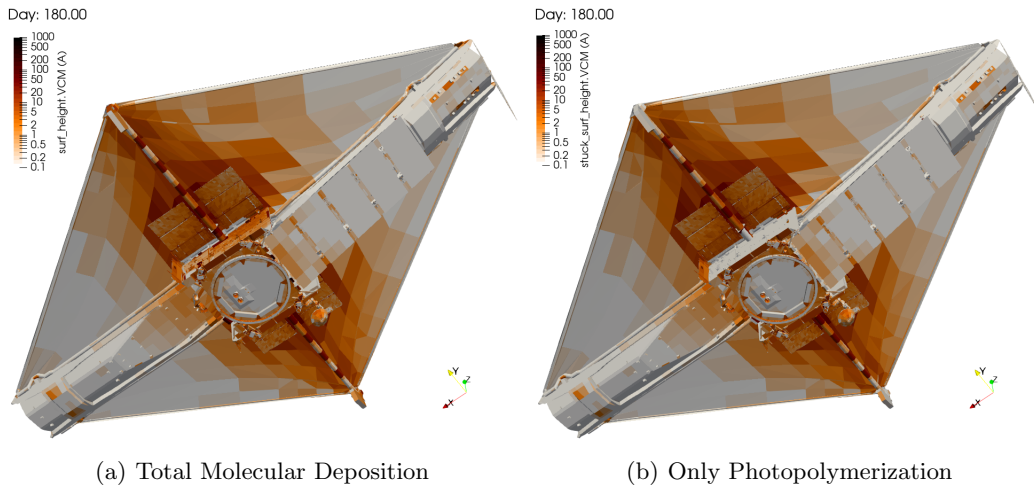
Figure 15. Molecular contaminant deposition thickness after 180 days, alternate view.

6.2 Molecular Contamination

Figure 14 displays molecular contaminant deposition thickness after 180 days. As discussed previously in Section 4.2, molecular deposition is composed of two contributions: cold temperature sticking and photopolymerization. Plot 14(a) shows the total VCM deposition thickness, which includes both contributions. Plot 14(b) visualizes solely the contribution from photopolymerization. As expected, we see that on the shadowed observatory side, the majority of the VCM population arises from cold temperature sticking. Photopolymerization is limited to the side faces of the primary mirror support structure as these faces have a view of the sun prior to the sunshield deployment. On the sun-facing side, shown in Figure 15, we can observe that the plots of total and photopolymerization-only deposition are almost identical. This side is too warm to sustain any deposition due to residence time, outside of few areas shadowed by the solar array or radiators. As a result, the VCM contamination loading on the sun-facing spacecraft side arises almost completely from photopolymerization.

7. CONCLUSION

In this paper we summarized a recently completed analysis of water ice and molecular contaminant redistribution during the commissioning phase of JWST. The analysis utilized 17 different geometry files with the solution advanced forward through discrete time steps. The existing surface deposition was mapped to the new geometry

configuration using corresponding element IDs whenever a stage transition was encountered. Surface temperature was obtained from a thermal solver solution. The probability of a molecule depositing to an impacted surface was computed from Murphy-Koop partial pressure relationship for water vapor, and from a temperature based sticking coefficient for VCM. In the case of VCM, we also accounted for photopolymerization on sun-facing surfaces. Selected subset of the computed results were presented. Our analysis predicted contaminant deposition levels compatible with the cleanliness requirements specified in the mission contamination control plan.

ACKNOWLEDGMENTS

REFERENCES

[1] "JWST contamination sources and effects analysis," tech. rep., NASA, 2012. JWST-ANYS-019440.

[2] T. Panczak, S. Rickman, L. Fried, and M. Welch, "Thermal synthesizer system: an integrated approach to spacecraft thermal analysis," *SAE transactions* , pp. 1851–1867, JSTOR, 1991.

[3] L. Brieda, "Numerical model for molecular and particulate contamination transport," *Journal of Spacecraft and Rockets* **56**(2), pp. 485–497, 2019.

[4] L. Brieda and M. Laugharn, "Optimization, development, and validation of the contamination transport simulation code," in *SPIE Optics & Photonics*, 2020.

[5] G. A. Bird and J. Brady, *Molecular gas dynamics and the direct simulation of gas flows*, vol. 5, Clarendon Press Oxford, 1994.

[6] C. Birdsall and A. Langdon, *Plasma physics via computer simulation*, Institute of Physics Publishing, 2000.

[7] D. M. Murphy and T. Koop, "Review of the vapour pressures of ice and supercooled water for atmospheric applications," *Quarterly Journal of the Royal Meteorological Society: A journal of the atmospheric sciences, applied meteorology and physical oceanography* **131**(608), pp. 1539–1565, 2005.

[8] D. Hall and T. Steward, "Photo-enhanced spacecraft contamination deposition," in *20th AIAA Thermophysics Conferece*, (Williamsburg, VA), 1985.